doi:10.26443/seismica.v5i2.2034

SEISMICA

Quantifying the erasure of earthquakes in desert landscapes

Malinda G. Zuckerman * [1], **Alba M. Rodríguez Padilla** [2,3], **J Ramón Arrowsmith** [1]

[1]School of Earth and Space Exploration, Arizona State University, Tempe, AZ, USA, [2]Division of Geological and Planetary Sciences, California Institute of Technology, Pasadena, CA, USA, [3]Now at Department of Geosciences, Utah State University, Logan, UT, USA

Author contributions: *Conceptualization*: A. M. Rodriguez Padilla, J R. Arrowsmith, M. Zuckerman. *Methodology*: A. M. Rodriguez Padilla, M. Zuckerman, J R. Arrowsmith. *Software*: A. M. Rodriguez Padilla, M. Zuckerman, J R. Arrowsmith. *Data Curation*: M. Zuckerman. *Formal Analysis*: M. Zuckerman, A. M. Rodriguez Padilla, J R. Arrowsmith. *Investigation*: M. Zuckerman, A. M. Rodriguez Padilla, J R. Arrowsmith. *Writing - Original draft*: M. Zuckerman, A. M. Rodriguez Padilla, J R. Arrowsmith. *Writing - Review & Editing*: M. Zuckerman, A. M. Rodriguez Padilla, J R. Arrowsmith. *Visualization*: M. Zuckerman, A. M. Rodriguez Padilla, J R. Arrowsmith. *Supervision*: A. M. Rodriguez Padilla, J R. Arrowsmith. *Funding acquisition*: A. M. Rodriguez Padilla, J R. Arrowsmith.

Abstract Seismic hazard analysis depends in part on understanding fault segmentation and slip distribution, which are partially recorded in the landscape during surface-rupturing earthquakes. Over time, surface processes degrade these features, challenging fault mapping. We use landscape evolution models to quantify this information loss in desert environments. Using post-earthquake lidar from the 2019 Ridgecrest (California) and 2010 El Mayor-Cucapah (Baja California) ruptures, we simulate landscape degradation using 2D linear diffusion in Landlab over 100, 1k, 5k, and 10k years, with a transport rate of 1 m^2/kyr. We assess change in mappable fault trace length, fault zone width, and a "degradation coefficient" based on topographic slope change. Field validation in 2024 (Ridgecrest) supports the modeled degradation. Results show that 20–80% of original fault trace length remains after 10k years and fault zone width decreases from a mean of 30 m to ~2 m, causing older rupture zones to appear narrower and less complex than initially. Degradation is fastest in the first 100 years, then slows. Fault zones with simple, single-strand morphology retain more mappable length and degrade more slowly. Fault zone structure primarily controls degradation rate and fault trace visibility. These findings provide quantitative constraints on landform degradation, informing probabilistic displacement hazard models and fault mapping in tectonically active regions.

Non-technical summary Large earthquakes create scarps and fractures that record the location of the fault and how the fault moved. These landforms are critical for reconstructing past ruptures and assessing seismic hazard, but they degrade over time as erosion and gravity smooth and erase them. We used high-resolution topography from the 2019 Ridgecrest (California) and 2010 El Mayor–Cucapah (Baja California) earthquakes to simulate how earthquake landscapes evolve in desert environments. Our results show that small, distributed scarps degrade rapidly, often disappearing within hundreds to thousands of years, while larger scarps persist longer but become narrower. This progressive loss of detail makes older rupture zones appear simpler and more localized than they originally were. As a result, fault maps based on degraded landforms likely underestimate rupture width and complexity. Recognizing this information loss is important for interpreting the geologic record and for improving fault displacement hazard models.

Production Editor:
Gareth Funning
Handling Editor:
Randolph Williams
Copy & Layout Editor:
Hannah F. Mark

Signed reviewer(s):
Christoph Grützner
Nadine Reitman

Received:
September 23, 2025
Accepted:
June 23, 2026
Published:
July 13, 2026

1 Introduction

Seismic hazard analysis relies on knowledge of the timing of past earthquakes, the length and segmentation of faults, the distribution of slip in past events, and the partitioning of that slip between primary and distributed fractures (e.g., Moss and Ross, 2011; Petersen et al., 2011; Youngs et al., 2003). Much of this information is recorded in the landscape coseismically and modified over time by surface processes and postseismic relaxation (Figure 1). While surface processes act immediately after each earthquake to alter the landscape, the geomorphology of a fault zone reflects the cumulative effects of multiple earthquakes over time (e.g., Wallace, 1990). The surface process clock starts ticking immediately after the earthquake (e.g., Arrowsmith and Rhodes, 1994; Wallace, 1990), so that the time elapsed since the most recent event and the surface process rates dictate the level of detail (or information) available for mapping the fault (Thompson Jobe and Reitman, 2025; Zinke et al., 2015).

In desert environments such as the Eastern California Shear Zone (ECSZ; Figure 2), relatively low surface process rates, limited vegetation, and moderate earthquake recurrence intervals together allow for much of the geomorphic signal from previous events to be preserved (e.g., Arrowsmith and Rhodes, 1994). Faults in the ECSZ are predominantly strike-slip. However, clear coseismic or small-scale lateral offsets are often difficult to identify in this region, particularly where continuous markers are absent. In such cases, vertical offsets expressed as scarps become a primary, lasting geomor-

*Corresponding author: mgzucker@asu.edu, malindazuckerman@gmail.com

phic indicator of faulting (e.g., Arrowsmith and Rhodes, 1994).

Fault mapping in the U.S. is informed by resources such as the U.S. Geological Survey Quaternary Fault and Fold Database (Schmitt et al., 2020). Faults that have recently ruptured are mapped as complex fault traces with apparently more distributed deformation than those that have not experienced an earthquake recently (Figure S1). Rupture databases (e.g., Nurminen et al., 2022; Sarmiento et al., 2025) capture an even higher degree of complexity of the fault trace and the amount and extent of distributed deformation, though the level of detail varies among earthquakes depending on data availability and mapping resolution. These discrepancies in mapped fault trace detail and complexity reflect more general issues: fault maps capture a time-integrated history of repeated rupture modified by surface processes. Surface processes control how long zones of deformation can be preserved in the landscape and how variability in coseismic vertical surface displacements translates into apparent geometric segmentation of the fault zone as the record is erased (e.g., Zinke et al., 2015).

Observations from the Monte Cristo Range in the Walker Lane (Nevada) illustrate that very distributed coseismic fracturing may leave little geomorphic expression over time, particularly in areas with few preexisting primary ruptures, highlighting how the landscape can quickly lose evidence of past earthquakes (Koehler et al., 2021). In this context, knowledge of fault trace complexity and degree of localization, and understanding how such information disappears from the landscape, is valuable for understanding fault zone damage and rupture mechanics. Constraints of the fault zone width are also essential for probabilistic fault displacement hazard analysis (PFDHA; Petersen et al., 2011; Scott et al., 2023; Zuckerman et al., 2026b).

Here, we focus on the ECSZ (Figure 2) for both expedience in terms of process understanding and activity of surface-rupturing earthquakes, as well as for potential application to hazard characterization for the region. We used a suite of 2D landscape evolution models to simulate and quantify the information loss associated with surface processes on earthquake rupture records in desert landscapes. 2D modeling (elevation z as a function of horizontal coordinates x and y) captures the spatial variability of fault scarps, including changes in height and continuity along strike. These features are not easily represented in a 1D (profile; elevation versus x) model. 2D modeling also allows for analysis of fault zone width and distributed deformation, making it better suited for assessing how secondary scarps and broader rupture patterns degrade over time, and how variable these patterns are along strike of the fault.

We rely on lidar and Structure from Motion (SfM) high-resolution topographic data covering the surface ruptures from the 2019 Ridgecrest (Hudnut et al., 2020; Zuckerman et al., 2025) and 2010 El Mayor-Cucapah (OpenTopography, 2010) earthquakes in the ECSZ. We considered sections of the rupture zones with different degrees of complexity (i.e., number of strands and fault geometry) and variable magnitudes of coseismic vertical offset. We simulated the effect of surface processes as transport-limited and diffusive with linear dependence on local topographic slope for the geomorphic transport law (Arrowsmith et al., 1998; Dietrich et al., 2003; Hanks et al., 1984; Hanks, 2000). We also briefly explored the effect of nonlinear transport laws, and we discuss that later in the manuscript (see Section 5.1; de' Michieli Vitturi and Arrowsmith, 2013; Ganti et al., 2012; Xu et al., 2021). More complex surface process idealizations beyond are possible (e.g., runoff-driven erosion and mass wasting); however, diffusion captures important changes across the landscape and balances conceptual clarity and computational expedience with sufficient process realism.

We ran the diffusion models using the open-access landscape evolution toolkit, Landlab (Barnhart et al., 2020; Hobley et al., 2017). We ran models from 0 to 10k years to examine the loss of information associated with the effect of surface processes and its implications for characterizing rupture hazard from faults without recent surface rupturing events, evaluating the output landscape at five different time steps. We supplemented these models with field observations and a SfM digital elevation model (DEM) collected four years after the 2019 Ridgecrest ruptures, which enable analysis of fine-scale landforms and examination of the model process and parameter choices. Our results suggest that the coseismic fault zones in the ECSZ are often more complex and broader than what remains visible in degraded desert landscapes, leading both remote and field mapping efforts undertaken many years post-earthquake to systematically underrepresent fault zone width, connectivity, and past fault displacement.

2 Data

We utilized 0.5 m/pix lidar-derived DEMs of the 2019 $M_w 7.1$ and $M_w 6.4$ Ridgecrest (Hudnut et al., 2020) and 2010 El Mayor-Cucapah (OpenTopography, 2010) earthquake ruptures (Figure 2). The Ridgecrest dataset was collected a month after the earthquake. The El Mayor-Cucapah dataset was collected four months after the event. For simplicity, we assume that little erosion occurred between the event and the data collection so that the post-earthquake lidar is representative of the coseismic distribution of surface ruptures and slip and represents the original forms of the faulted landscape. We also assume the effect of afterslip along the fault zone is negligible.

We selected rupture locations with visible vertical displacement (fault scarps) for detailed analysis. For Ridgecrest sites (R1-R10; Figure 2), we used a record of field observations and a rupture line shapefile (Ponti et al., 2020b,a). For El Mayor-Cucapah sites (E1-E10; Figure 2), we used rupture line shapefiles from the 2010 earthquake and the 1892 Laguna Salada earthquake to make sure we avoided composite scarps (Fletcher et al., 2014; Rockwell et al., 2015). At each location, we clipped ~120 x 140 m areas from the lidar DEMs, with the longer dimension loosely aligning with the fault trace.

We produced an SfM DEM collected four years after the 2019 Ridgecrest sequence along a portion of

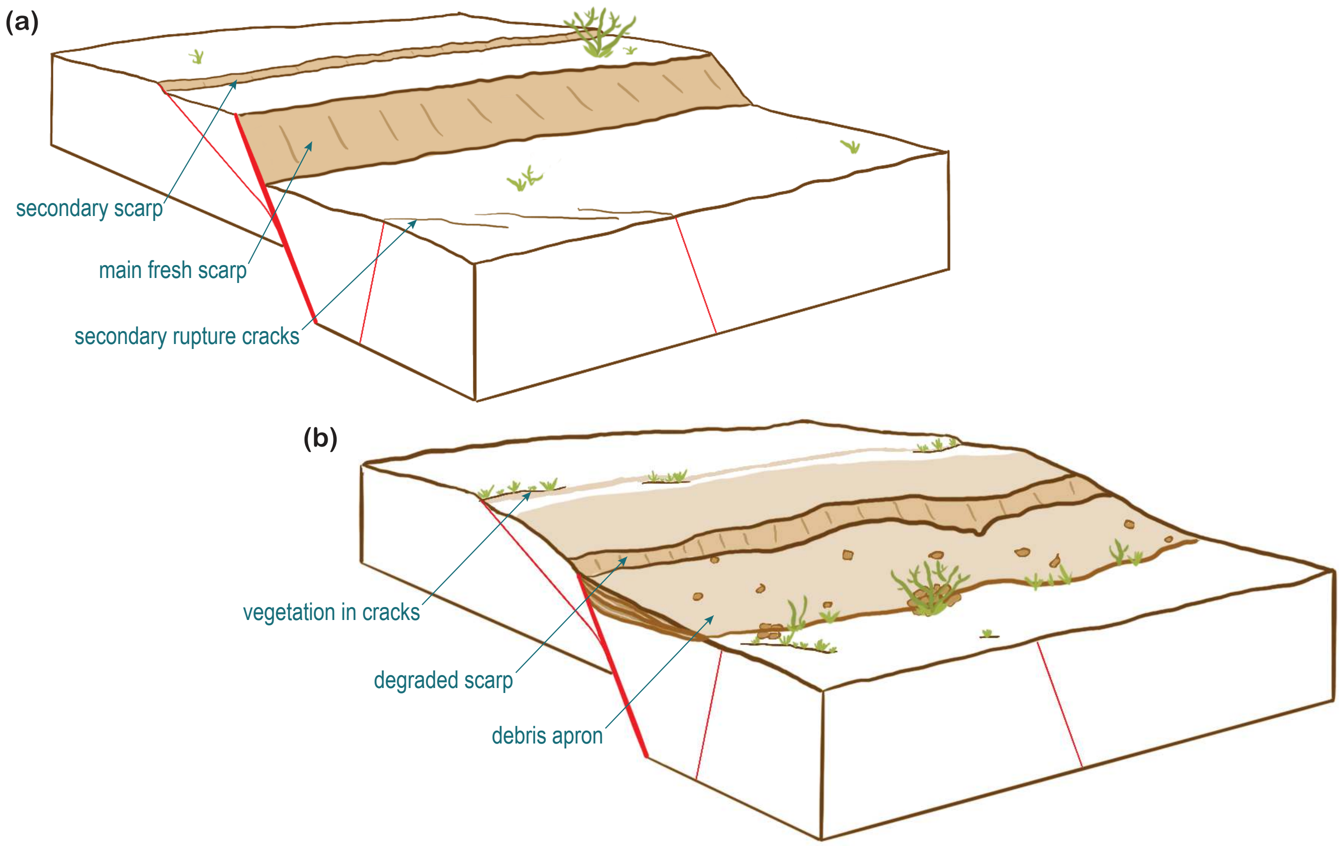

Figure 1 Surface processes act to remove evidence of earthquake ground rupture. A: A fresh primary coseismic scarp face with a secondary scarp above and cracks below. B: The degraded fault scarp after some time, with rounded edges and eroded and transported material. The secondary scarp and cracks have disappeared or have filled in with vegetation, indicating a loss of information about the original fault geometry. They persist in the subsurface. Primary (thick) and secondary faults (thin) are in red.

the $\mathrm{M_w}7.1$ ruptures (Zuckerman et al., 2025). Our 0.014 m/pix DEM shows degradation of the fault scarp due to rain and other surface processes. We also observed degradation due to anthropogenic processes (e.g., tracks in Figure 7), but do not consider it in our analysis.

3 Methods

3.1 Implementation of transport models for simulating landscape evolution

Surface processes, simplified as diffusive here, remove high-frequency signals from the landscape, smoothing the fine-scale structure of fault scarps and any additional tectonic and non-tectonic roughness. To investigate the impact of surface processes on the preservation of fault traces, we combine analysis of DEMs and their modifications simulated using surface process models. We limit our idealizations to those surfaces over which runoff is unimportant (thus, not considering debris flow or fluvial responses). We used the 2D (elevation z as a function of x and y) Landlab computation toolkit (Barnhart et al., 2020; Hobley et al., 2017). The continuity equations for transport-limited conditions are:

$$\frac{dz}{dt} = U - \nabla q_s \tag{1}$$

where $\frac{dz}{dt}$ is the change in elevation with time, U is rock uplift rate, which we assume is 0 given the relatively short interseismic timescales of interest, and q_s is the sediment transport rate, whose spatial divergence governs sediment continuity. The simplest transport law assumes that the processes are linearly dependent on local slope S (reduces to "diffusion erosion"; equation 2; Dietrich et al., 2003):

$$q_s = -kS \tag{2}$$

We used a linear diffusivity k of $1\ m^2/kyr$, a rate constant describing the efficiency of sediment transport by diffusive processes, which is appropriate for semiarid environments like the ECSZ (Hanks et al., 1984; Nash, 1984; Pierce and Colman, 1986; Hanks, 2000). We recognize that the morphologic age (the product of the diffusivity k and t, the duration of surface process operation or age of the feature) is the more fundamental measure of geomorphic change (e.g., Hanks, 2000). In other words, with this simple geomorphic model, a fault scarp with processes driven at $1\ m^2/kyr$ for 10 kyr would appear the same as one that had more vigorous ($10\ m^2/kyr$) processes operating for 1 kyr (Hanks et al., 1984). However, for ease of application to the ECSZ examples and translation into PFDHA, we have fixed k at $1\ m^2/kyr$ and changed t. We conducted all of our sim-

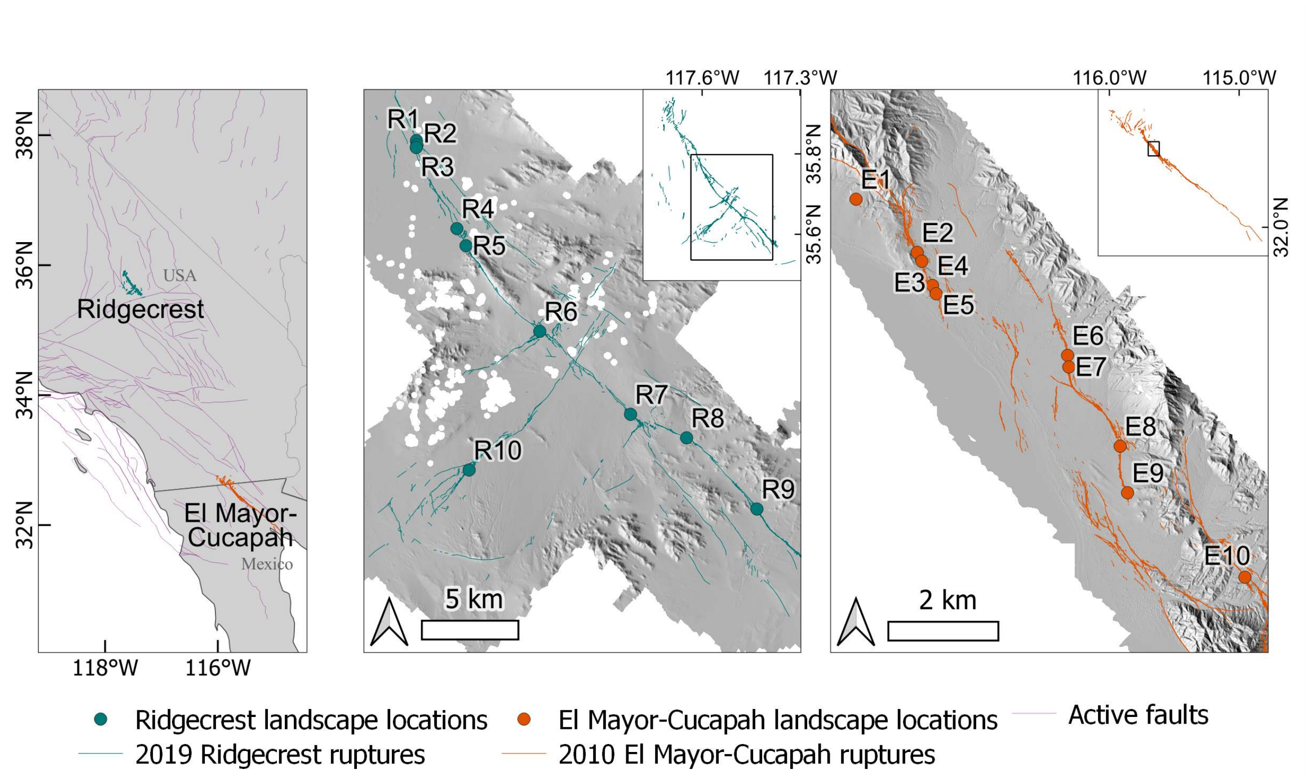

Figure 2 Analysis locations along the 2019 Ridgecrest (center) and 2010 El Mayor-Cucapah (right) ruptures. Topography: Ridgecrest (Hudnut et al., 2020); El Mayor-Cucapah (OpenTopography, 2010). Rupture traces: Ridgecrest (Ponti et al., 2020a); El Mayor-Cucapah (Sarmiento et al., 2024).

ulations using linear diffusion as a simplifying approximation. Many applications, especially for young and steeper scarps, are better idealized with a nonlinear dependence of transport rate on local slope up to a critical slope (S_c; typical values of ~1; equation 3; sensu Ganti et al., 2012):

$$q_s = -kS(1 + (\frac{s}{s_c})^2) \tag{3}$$

Thus, we also ran a subset of simulations using Landlab's implementation of the nonlinear soil flux approximation from Ganti et al. (2012) and compared the model outputs from the linear and nonlinear transport laws (see discussion; Section 5.1).

3.2 Mapping of diffused synthetic digital elevation models

To explore the qualitative change in mappable capacity due to scarp degradation, we mapped surface ruptures on shaded relief basemaps of the post-diffusion DEMs at simulated time intervals (0, 100, 1000, 5000, and 10000 years) post-earthquake. We performed this exercise from the most to least diffused time interval of our model output DEMs to minimize the effect of prior knowledge. The mapping was completed by one person. From the mapped fault traces, we examined how fault geometry, segmentation, and the amount of resolvable distributed deformation change with time from each original configuration.

At each diffusion time step, we mapped fault traces with QGIS (qgis.org) software following a geomorphology-based systematic mapping approach (Figure 3; Adam et al., 2025; Scott et al., 2023; Zuckerman et al., 2026b):

1. **Preliminary mapping**. We created hillshade and slope derivatives and topographic profiles from the DEMs. We mapped the morphology of each DEM using the derivative maps and profiles by tracing observed topographic convexities and concavities.

2. **Map geomorphic indicators of active faulting.** We placed points where features show evidence of faulting in the landscape (e.g., fault scarp, lineation in topography, linear valley/drainage).

3. **Map fault traces.** We identified and mapped the fault traces using the morphological map with geomorphic indicators. We placed the fault trace lines at the midline between the scarp base and head. We added a confidence level to each fault trace segment.

For the first five mapping areas, we explicitly saved each mapping step of the method as a shapefile to ensure consistency across sites. For the remaining locations, we only recorded the faults in shapefiles, keeping steps 1 and 2 implicit (fault traces in Figure 3).

3.3 Quantifying the erasure of surface ruptures from landscape evolution: degradation coefficient, mappable length, and fault zone width

To quantify information loss, we define three metrics based on the diffused DEMs: a slope change coefficient,

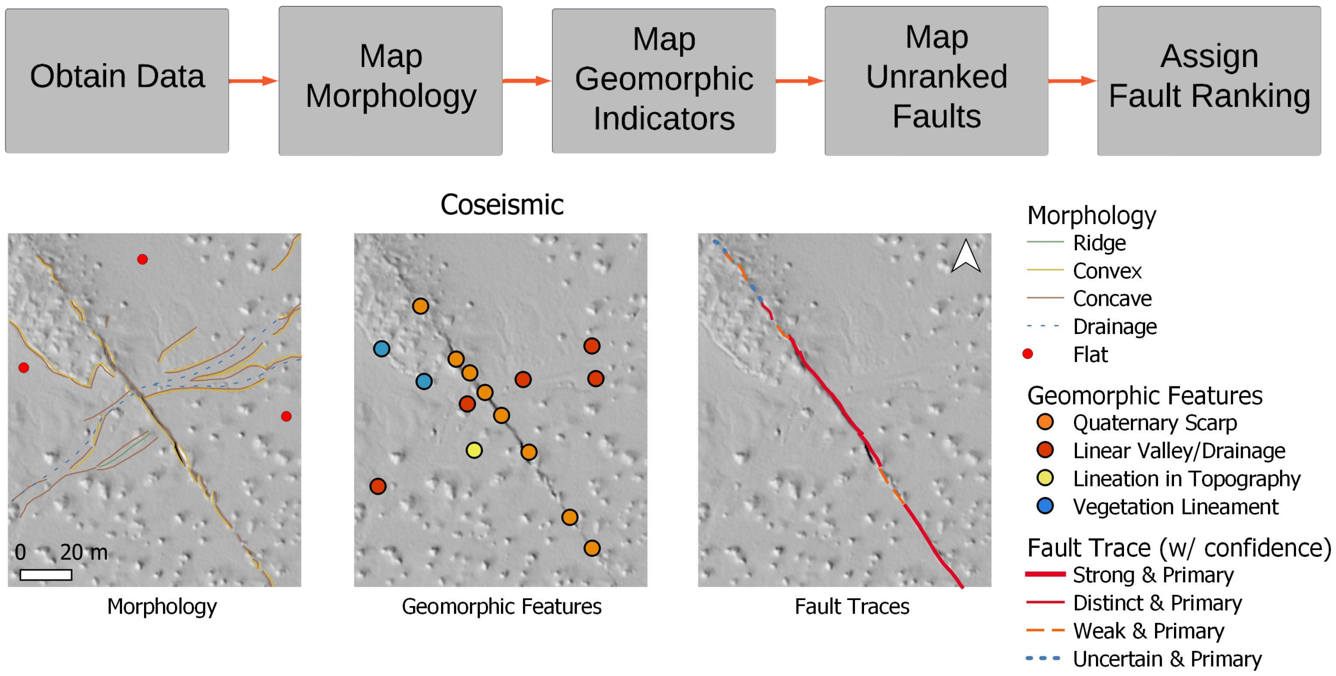

Figure 3 Mapping process flow diagram and demonstration. We follow a systematic fault mapping process (Adam et al., 2025; Scott et al., 2023; Zuckerman et al., 2026b) to consistently record mappable fault line length.

mappable fault trace length, and fault zone width. By definition, elevation change with time is scaled by local topographic curvature. Sharp parts of the landscape smooth most rapidly. The diffusion preferentially diminishes steep slopes in the landscape and decreases the mean of and narrows the slope distribution (Figures 4–6). To visualize information loss, we chose a simple topographic metric. We define the slope change coefficient ϕ as the ratio of the 68th percentiles of the slope distributions S at $t = t_0$, i.e., the moment of scarp creation (in practical terms, the moment when the topography data were collected) and $t = t_i$:

$$\phi = \frac{S_{68,t_0}}{S_{68,t_i}} \tag{4}$$

From the fault traces of the surface ruptures, we computed the mapped lengths at each step for which we simulated landscape evolution. For comparison across different sites, we normalize the mapped length at a given time by the initial length, estimating the remaining fraction of the original mappable surface rupture immediately after the event. We also computed the width of the mappable fault zones by finding the widest distances between mapped faults with the same strike.

4 Results

4.1 Landscape evolution over 10 ky based on linear diffusion

To graphically illustrate the loss of information due to diffusion, we present two examples (see Supplementary Material for results from all 20 locations). The first (R6) is a single fault trace in a simple, relatively flat landscape (Figure 4). The second example (E10) is a more complex rupture cutting a higher relief, channelized landscape (Figure 5). For each landscape, we show degraded hillshades, mapped fault trace line length and fault zone width, elevation change, and slope distribution evolution (and ϕ) for each time step (0, 100, 1000, 5000, 10000 years with $k = 1\, m^2/kyr$).

We start with a simple fault trace in a landscape from the $\mathrm{M_w}7.1$ 2019 Ridgecrest earthquake (Figure 4). There is one primary trace and limited secondary faulting. Fault zone width narrows from ~5 m to a single strand (0.1 m minimum thickness) over time. Mapped fault trace line length decreases over time, with each timestep losing between 7–17 m. By 10 kyr, 28% of the original mapped line length is lost. The rate of loss of mappable line length is greatest in the first time steps.

The slope change coefficient increases with time and diffusive effects until the last time step, 5–10 kyr. There is a more significant effect from diffusion at the first time step, with about a 40% change in ϕ, than at other time steps, where ϕ changes between 4 and 13%. Section 4.2 explores the effects of the pre-faulted landscape roughness and DEM dimensions on ϕ. We note that much of the topographic roughness in this example comes from bushes and boulders, which complicates the interpretation of the change in ϕ in its current form (see Section 4.2).

A more complex example is site E10 from the $\mathrm{M_w}7.2$ 2010 El Mayor-Cucapah earthquake (Figure 5). There are multiple fault strands with different vergence, and the landscape has abundant fluvial landforms. Mapped line length decreased significantly: a 77% loss from 1–10 kyr. Loss of mappable line length varies from 27–205 m between timesteps. The largest difference is between 100 and 1000 years. Fault zone width narrows from about 45 m to a single strand.

The slope change coefficient for the second example increases from 0–1 kyr, then decreases. The highest rate

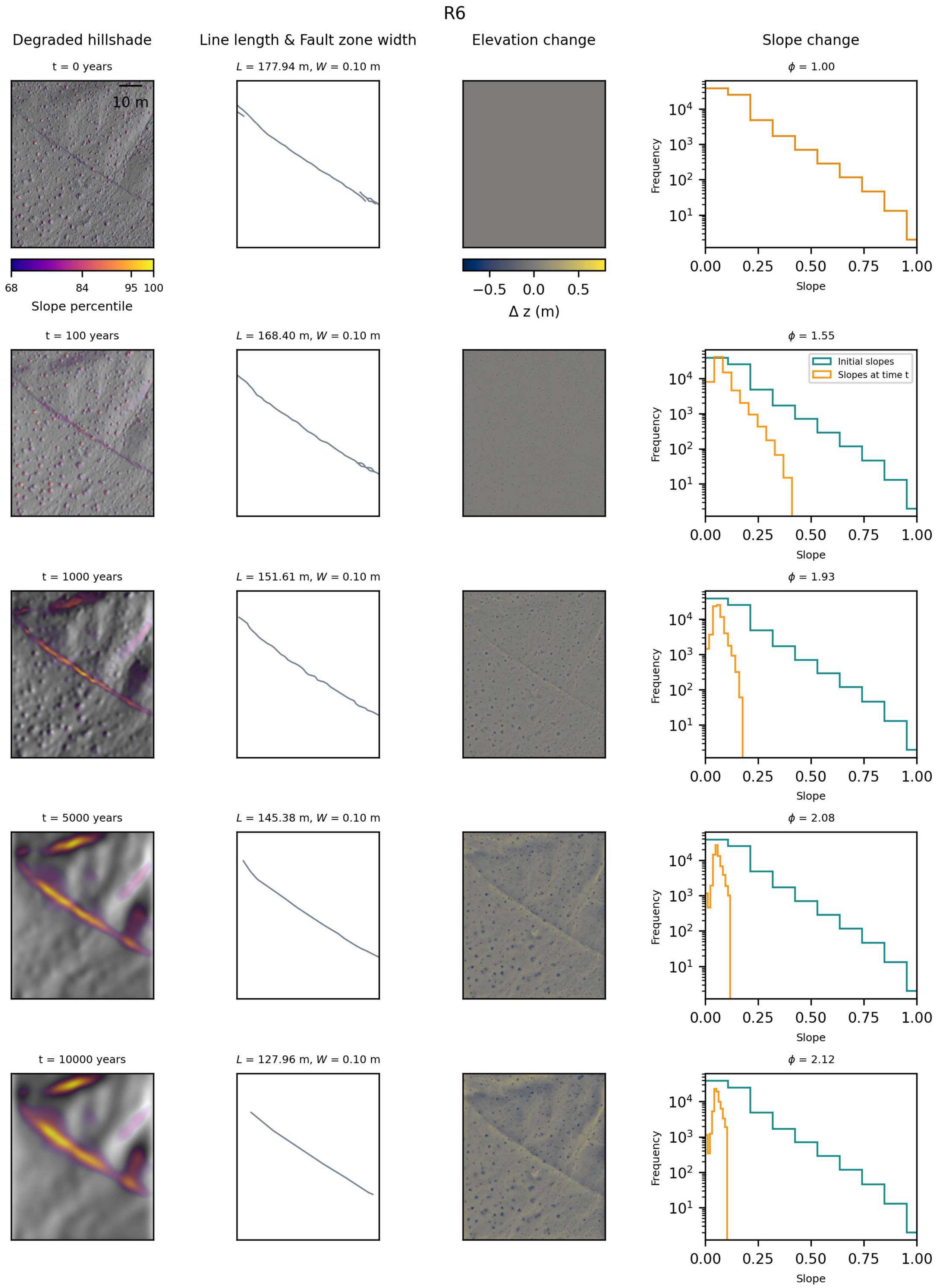

Figure 4 Simple fault trace degradation example. Landscape R6 from the $\mathrm{M_w}7.1$ 2019 Ridgecrest earthquake (see location in Figure 2). Columns from left to right: degraded hillshade with slopes above the 68th percentile highlighted, mapped line length and maximum fault zone width (orange line), elevation change, and slope change (including the degradation coefficient, ϕ). Slopes across the entire landscape are included. Rows represent time steps at which landscapes were linearly diffused. A minimum fault zone width of 0.1 m was imposed to avoid undefined values on the logarithmic scale in later analysis.

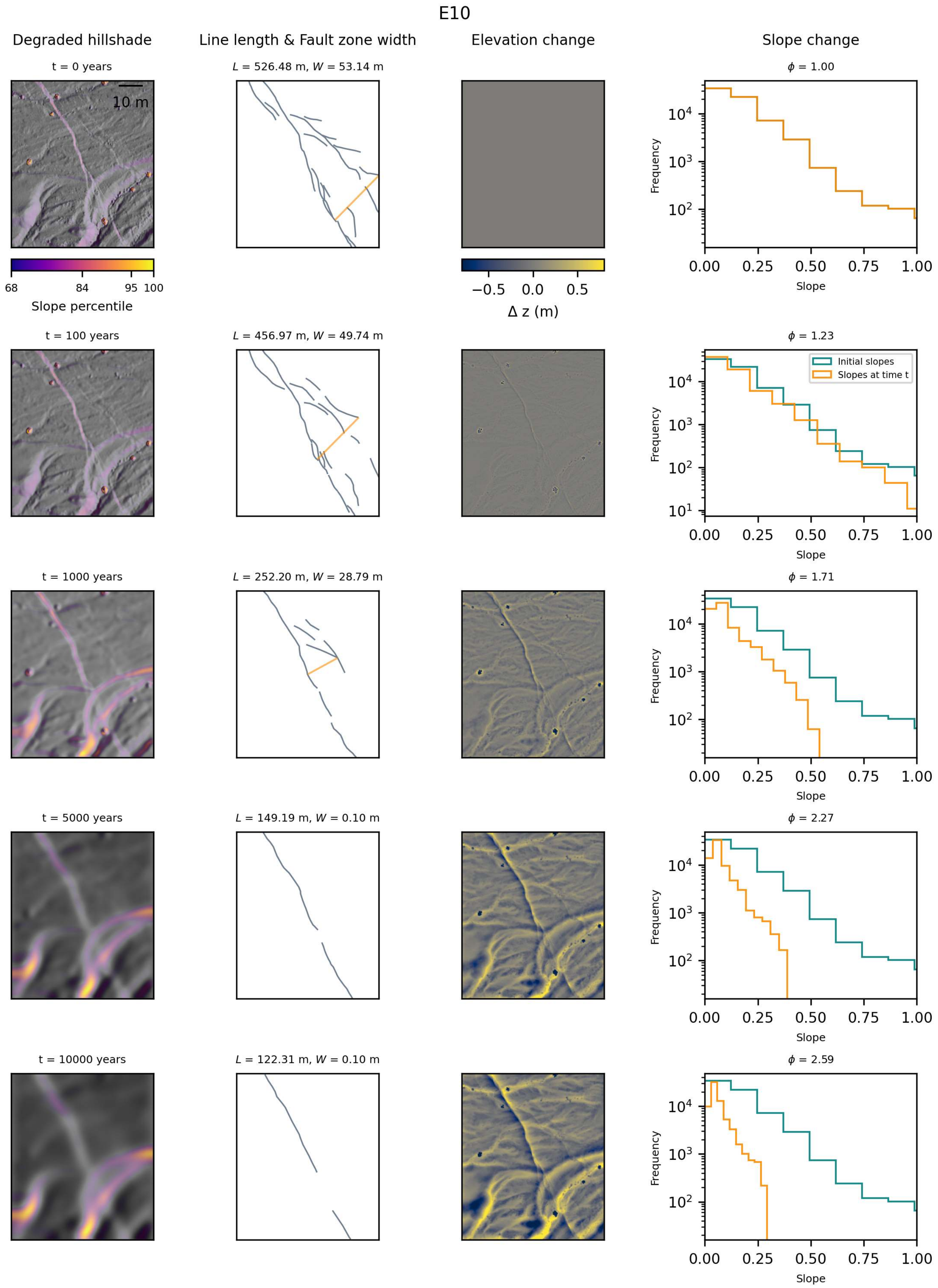

Figure 5 Complex fault trace degradation example. Landscape E10 from the 2010 El Mayor-Cucapah earthquake (see location in Figure 2).Columns from left to right: degraded hillshade with slopes above the 68th percentile highlighted, mapped line length and maximum fault zone width (orange line), elevation change, and slope change (including the degradation coefficient, ϕ). Slopes across the entire landscape are included. Rows represent time steps at which landscapes were linearly diffused. A minimum fault zone width of 0.1 m was imposed to avoid undefined values on the logarithmic scale in later analysis.

of degradation is between initial and 1 kyr. More information is lost earlier when the curvature and landscape complexity are higher, which differs from when the most mappable information is lost, as described by line length.

4.2 Evolution of the slope change coefficient, mappable line length, and fault zone width

In this section, we summarize the results of all the models. They encompassed 20 sites (10 from El Mayor-Cucapah and 10 from Ridgecrest), and we degraded the landscapes at 5 timesteps (0, 100, 1000, 5000, 10000 years; 100 model results in total—see repository; Zuckerman et al., 2025). All simulations were linearly diffused with a k of $1\ m^2/kyr$. The line length, fault zone width, and ϕ evolution demonstrate the loss of information about the fault zone trace geometry and continuity. We note, in particular, the diminished evidence for the secondary traces in the degraded landscape (e.g., Figure 1). Figure 6 summarizes the results.

The mapped line length loss from all analysis locations exhibits a wide range, from only 20% of the original length captured at time 10 kyr to over 70% (Figure 6A/D). There is also variation in how quickly the remaining mapped line length decreases. A few landscapes lose mappable line length gradually, while most others lose significantly more information in the first time step than in the following steps. Variation most likely stems from differences in the sharpness of the original forms in different landscapes, with more change occurring quickly in sharper, more defined fault scarps with arrays of smaller scarps along distributed traces. In general, the remaining line length decreases with time, as shown by the mean of the populations at each time step (Figure 6A).

The slope change coefficient, ϕ, is a simple metric that captures the change in slope distribution from the landscapes. ϕ increases over time nonlinearly, as expected from the diffusion modeling, with more change occurring in the first 100 years (Figure 6B/E). As a population of landscapes, the mean of ϕ increases through time (Figure 6B). However, there is also a wider variation in ϕ through time, as shown by the increasing width of the curves in the PDFs (Figure 6E).

We choose equations to describe the evolution of the degradation coefficient, the fault zone width, and the mappable fault length based on analytical convenience. We fit the evolution of ϕ with the following nonlinear relationship,

$$\phi(t) = ct^a \tag{5}$$

where t is time (years), $\phi(t)$ is the slope change coefficient at time t, and a and c are fit for each landscape. This analytically convenient relationship captures the nonlinear evolution of ϕ over time well (Figure 6B). We fit the evolution of the remaining mappable line length, $L(t)$, as a nonlinear function of time:

$$L(t) = m - \frac{nt}{t+p} \tag{6}$$

where t is time (years), $L(t)$ is mappable line length (meters); and m, n, and p are fitting parameters. This simple relationship captures the range of evolution observed in the different datasets: locations with initially simple fault traces lose mappable line length steadily and linearly, whereas locations with high degrees of complexity lose information rapidly and nonlinearly (teal and orange lines in Figure 6A, respectively). The nonlinear decay becomes steady when the bulk of the distributed deformation has been erased, and only a primary trace is left. Because distributed deformation is generally accommodated along smaller scarps with lower displacements, the erasure of these features represents a large decrease in line length but not in ϕ. This is an important limitation of ϕ and highlights the value of the line length assessment.

The observed DEMs contain additional roughness elements besides the fault scarps (bushes, boulders, fluvial and alluvial fan elements). Because we diffused the entire landscape, we must consider that the change in slope distribution and thus ϕ describes not only the fault scarp degradation but also the potentially unrealistic smoothing of those other topographic elements in the DEM (Figures 4 & 5, third column). Thus, ϕ may only crudely capture the loss of information. This effect may deflate the 68^{th} percentile of the slopes used to calculate ϕ by including the smoothing of non-tectonic slopes. We recognize that at least the vegetation roughness is likely to be stochastically renewed with time. Because the landscapes ruptured by the Ridgecrest and El Mayor-Cucapah earthquakes are similar, this bias is systematic in all measurements and does not prevent comparison across sites. In Section 5.2, we explore the effect of noise renewal in the landscape on the slope change coefficient with synthetic DEMs. Conversely, including flat areas adjacent to the scarp could increase uncertainty by yielding a lower ϕ. By keeping consistent DEM dimensions around the scarps, we mitigate this bias, enabling consistent comparison across sites (but with diminished sensitivity). Importantly, if our metrics were to be used for landscapes with different pre-faulted slope distributions than those at Ridgecrest and El Mayor-Cucapah (e.g., a more vegetated, fluvially modified, or bedrock-dominated area), ϕ would have to be re-interpreted in that context.

To assess how fault zone width evolves with surface degradation, we measured the maximum width between mapped fault traces that share a similar strike direction (orange line in Figures 5 and 6). This width represents the spatial extent of recognizable surface rupture and provides a simple proxy for how much of the original rupture complexity remains visible over time. We fit the evolution of fault zone width with:

$$W(t) = m + n \ln\left(\frac{t}{p}\right) \tag{7}$$

where $W(t)$ is fault zone width (meters) at time t (years), and m, n, and p are fitting parameters.

Figures 6C & F show that fault zone width decreases markedly with time. Individual site measurements exhibit high variability at early time steps (0–1000 years), with widths ranging from less than 10 m to over 90 m.

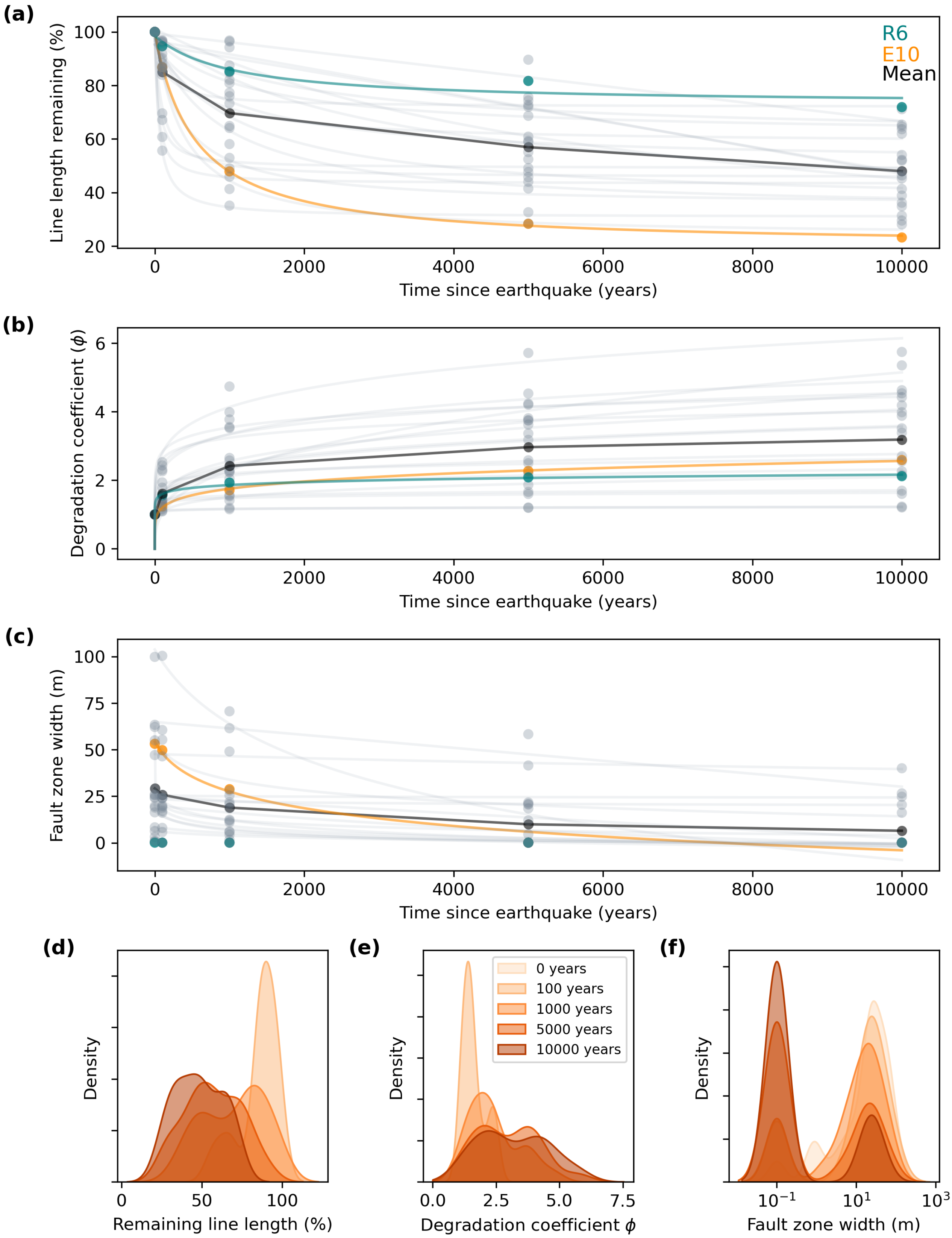

Figure 6 Evolution of mappable line length, ϕ, and fault zone width for all modeled landscapes (see locations in Figure 2 and data in the repository). A/B/C: Percentage of mapped line length remaining (A), ϕ (B), and fault zone width (C) for all landscapes at each time step. The scattered dots represent our measurements, and the lines are nonlinear fits to the evolution over time. R6 (Figure 3, teal) and E10 (Figure 4, orange) illustrate relatively simple and complex cases, respectively. We include the mean of all landscapes for a given timestep in black. There is no line fit for R6 due to the fault zone width being only one trace. D: Probability density functions (PDF) of the remaining line length (%) for each model output time step. Each PDF includes the remaining line length measured for the twenty models at that time step. E: PDFs of ϕ (equation 4) estimated for each model output per time step. We use a Gaussian kernel with smoothing of 0.8 in seaborn (Waskom, 2021). F: PDFs of fault zone width at all mappable fault locations for each time step.

By 10,000 years, fault zone widths converge to narrower values, often down to one fault trace. The mean fault zone width (Figure 6C) declines from 30 m to approximately 7 m over the 10,000-year time steps (on rare occasions, fault zone width increases in some time steps due to the reduction in resolution for mapping).

4.3 Field observations of four years of landscape evolution in Ridgecrest, CA

Immediately after the 2019 Ridgecrest earthquake sequence, scientists documented the ruptures in detail through fieldwork and high-resolution imagery (e.g., Brandenberg et al., 2020; DuRoss et al., 2020; Pierce et al., 2020; Rodriguez Padilla et al., 2022; Young et al., 2024). They documented discontinuous, subparallel cracking and scarps ranging from 10–70 cm high. The ruptures stepped up to hundreds of meters and formed both compressional and tensional features like thrusts and grabens.

We traveled to Ridgecrest in April 2024 to observe initial modifications of the original forms of the ruptured landscape. We collected uncrewed aerial vehicle (UAV) imagery along the $M_w 7.1$ ruptures in areas with noticeable vertical displacement and good accessibility (35°38'48" N, 117°28'45" W). Using SfM (Johnson et al., 2014), we created a 0.014 m/pix DEM (Figure 7; Zuckerman et al., 2025).

During our visit in 2024, we noticed modest degradation of the original ruptured landforms. The primary fault scarp is still visible and continuous (Figure 7A–D). However, the main scarp has been softened and lacks sharp edges. There was abundant evidence of gravity-driven scarp collapse at the base of the scarp throughout. Vegetation has grown back over and into the scarp (Figure 7A–C), emphasized by our field campaign occurring during spring (April 2024). The scarp has been variably modified by diffusive processes, sheetwash, overland flow, and rilling. Distributed fracturing is still visible, though eroded and overgrown with vegetation. Most of the finer-scale distributed fractures at this site have been filled in by wind-blown sediment, but remain apparent by the narrow rows of vegetation growing within them.

Where the rupture diverges into more than one trace, the scarps are smaller, less sharp, and less continuous (Figure 7D right inset). These smaller scarps will degrade sooner, meaning the evidence of those ruptures and their distributed trace geometry will be lost more quickly than the taller scarps. Consequently, in 1000 years, a geologist might conclude there was only one trace there while, in actuality, the fault zone was wider. In 2019, the original forms at this locale were quite complex, often not forming a single strand. The mapped rupture dataset of Ponti et al. (2020a) documents a parallel strand at this location that is barely detectable on our DEM, further illustrating how secondary ruptures can become nearly invisible within just a few years of the earthquake (Figure 7). When looking back at scarps beyond 1000 years (or more generally, $kt > 10^3 m^2$), we should consider that a wider fault zone and additional secondary rupturing may have been lost to degradation.

5 Discussion

5.1 Effect of diffusion model choice (or, more broadly, surface process idealization)

For simplicity, we purposely chose to linearly diffuse the 20 landscapes. Nonlinear diffusion is thought to be more consistent with the effects of surface processes on young fault scarps because soil flux increases nonlinearly with steeper slopes (compare equations 2 and 3; Figures 8 & 9; Andrews and Hanks, 1985; Roering et al., 1999), and new fault scarps are steeper and sharper. In general, landforms with large morphologic ages will be degraded to converge to similar forms regardless of the diffusion idealization. Thus, the nonlinear effects would be more significant for relatively younger features (Figure 9). Nevertheless, our conclusions about the loss of information in terms of line length and ϕ are demonstrated adequately with the simplifying linear assumption (see also Gray et al., 2025).

We assessed nonlinear solutions by comparing model outputs from the linear and nonlinear transport laws (Figures 8 & 9). After performing our fault mapping (Figure 3) on the nonlinear outputs, we found negligible differences in results for the landscapes studied. In part, this is due to the relatively modest changes from low morphologic ages and the smaller nonlinear effect from the Ganti et al. (2012) idealization (as opposed to that suggested by Andrews and Hanks (1985) and implemented by de' Michieli Vitturi and Arrowsmith (2013); Roering et al. (1999); etc.). In the latter case:

$$q_s = \frac{kS}{(1 - S/S_c)^n} \quad \text{(compare to equation 3; Figure 8)} \tag{8}$$

Because slopes in our study are well below the critical threshold, nonlinear effects are minimal, so the linear model is a reasonable choice for our goal of illustrating diffusion-driven information loss. (Figure 8).

In the future, studies of larger scarps or those in environments with a thicker soil mantle or bare bedrock could assess fault scarp degradation using depth-dependent and nonlinear geomorphic idealizations (e.g., Arrowsmith et al., 1996; Johnstone and Hilley, 2015). This is important to determine the effects of different rock types and their conversion to regolith. Depth-dependent diffusion modeling could also be used to explore the effects of surface processes on buried faulting.

When idealizing surface processes, we also recognize that other surface process changes can additionally alter how tectonic geomorphic features like fault scarps reflect (or do not) past seismic activity. Nonlocal idealizations (e.g., Gray et al., 2025) account for processes involving greater particle motions than the diffusive idealization–important early in the scarp evolution–such as ravel and sheetwash. Nevertheless, for simplicity we chose the diffusion implementation. And, at larger timescales, the details of the implementation matter less as the forms smooth and information is lost. In addition, Reitman et al. (2019) included a 2D displacement field to include the width of the shear

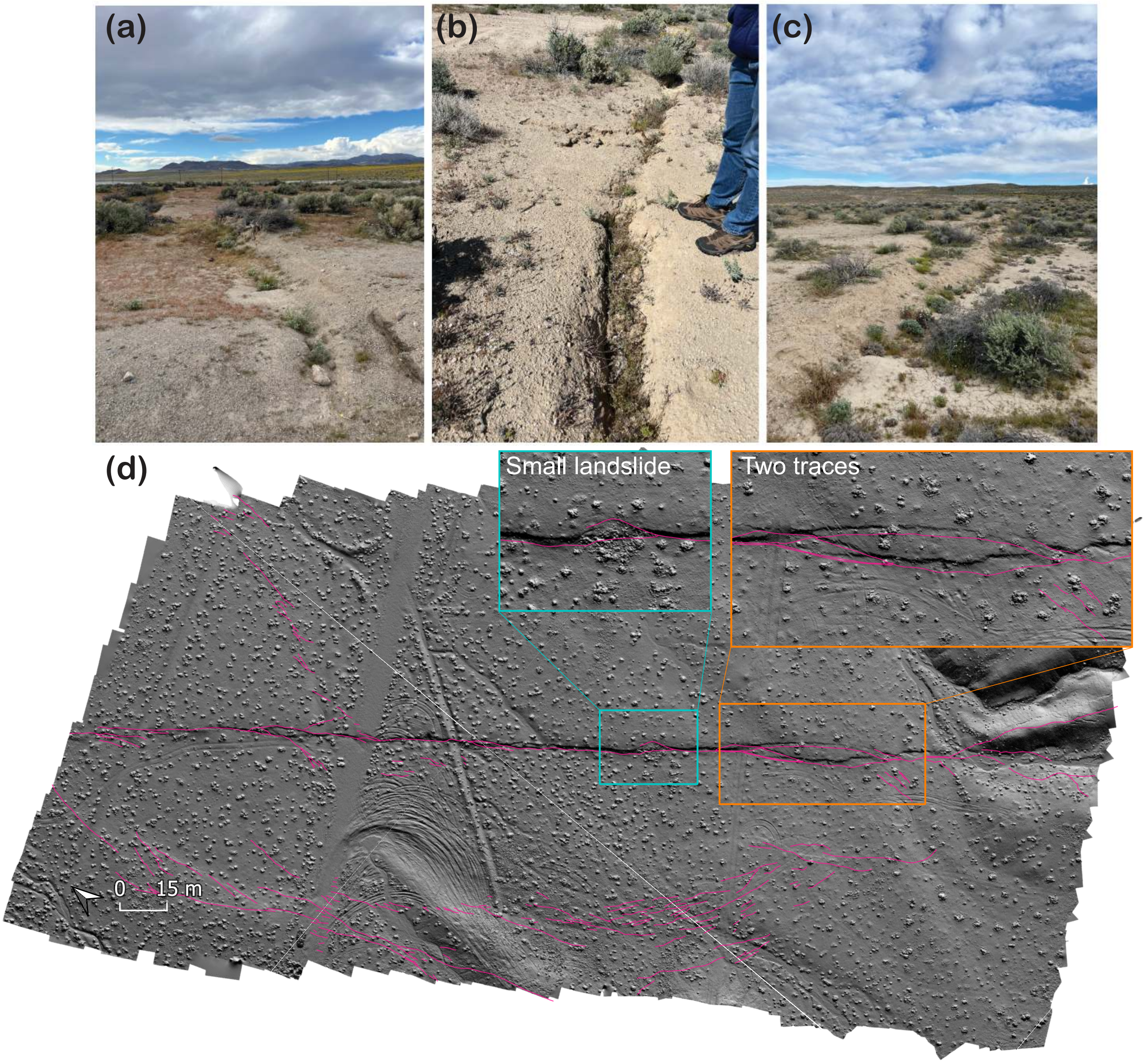

Figure 7 Scarp degradation 4.5 years after the Ridgecrest 2019 earthquakes. (A–C) Vegetation has occupied many cracks, and the primary scarp, though smoothed, remains visible. (D) 0.014 m/pix DEM of the visible fault trace (UAV and SfM; 35°38'48" N, 117°28'45" W; Zuckerman et al., 2025). The imagery was collected in April 2024. Mapped surface ruptures from Ponti et al. (2020a) are shown in magenta.

zone in their offset-channel-focused landscape evolution model. Along with diffusion operating over hillslopes with low drainage area, they implemented a full bedrock channel fluvial scheme to simulate landscape evolution across a strike-slip shear zone. They warn that the degradation of offset markers may lead to misinterpretation of earthquake frequency and magnitude. Offset measurements systematically underestimate true displacement unless fault zones are less than 5 m wide and measurements are taken shortly after an earthquake. These results further exhibit the need to quantify how landscapes degrade over time.

Our models simulate diffusive processes on vertical scarps from predominantly strike-slip earthquakes. This was the product of choosing to focus on the effect of surface processes in eroding scarps in the desert landscapes of southern California and northern Mexico. This work could be expanded to normal faults under some considerations. Because coseismic normal fault scarps tend to be taller than the vertical scarps resulting from strike-slip events, non-linear diffusion will appropriately describe the system for a longer time period than for strike-slip faults, meaning our linear approximation would be less appropriate over a longer timescale in the early years after an event.

5.2 Effect of random geomorphic elements and vegetation on degradation metrics

To better understand how non-tectonic roughness, particularly vegetation, may influence our degradation metrics, we conducted a set of synthetic tests. We generated a synthetic landscape with a single central scarp (testing 1, 2, 3, 4, and 5 m-high scarps) and applied our

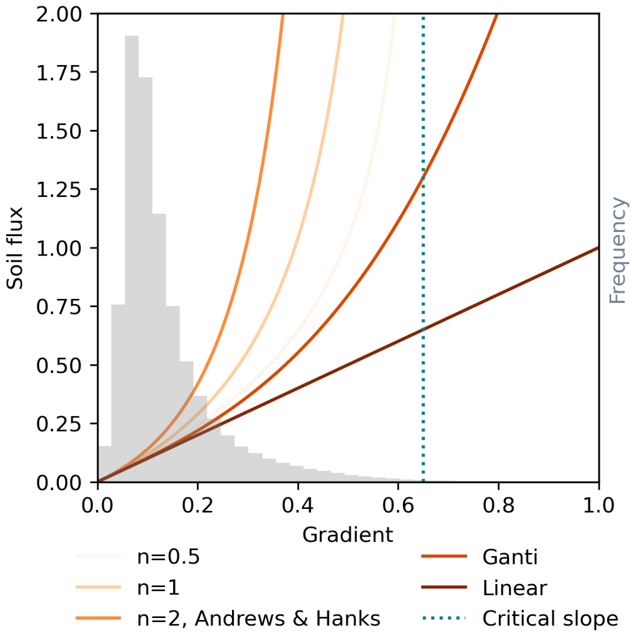

Figure 8 Soil flux as a function of slope under different diffusion idealizations (equations 3 and 8; Andrews and Hanks, 1985; Ganti et al., 2012). The gray histogram shows the distribution of slopes in our $t = 0$ landscape DEMs (i.e., the post-earthquake lidar data).

linear diffusion model over time (Figure 10). At each timestep, we added new random noise to the surface (noise renewal), with an amplitude equal to 1% of the scarp height, added at every modeled time step. This approach simulates the variable influence of sparse vegetation or geomorphic elements such as cobbles or small bushes, consistent with hyperarid environments like the ECSZ. It is not intended to represent denser or larger vegetation found in more humid settings.

By introducing new surface roughness at each time step, we test the robustness of ϕ under stochastic surface conditions, such as the growth and death of vegetation. When noise renewal is included, ϕ is larger for small scarps than tall scarps at late timesteps (Figure 10B), because renewed noise dominates the slope distribution relative to the scarp signal for small scarps. In contrast, without noise renewal (Figure 10C), small and large scarps become essentially indistinguishable, as other features in the landscape are also diffused. We calculate ϕ across the entire DEM rather than in a window around the scarp, so that it could serve as a reconnaissance tool for assessing landscape degradation state without prior knowledge of scarp location. This makes ϕ less sensitive for small scarps in noisy landscapes, and we acknowledge this as a limitation of the metric in its current form. Nevertheless, ϕ can reflect tectonic signal loss at the landscape scale and remains a useful first-order metric for assessing degradation state (Figures 4–6). Unlike vegetation roughness, erosional features such as rills and new channels that develop over time locally increase slope and are not captured by our noise renewal tests, meaning ϕ may be further complicated in landscapes undergoing active erosion. Geomorphic features such as boulders and cobbles represent a third category — neither stochastically renewed nor erosionally modified. These features contribute persistent background roughness that changes only on very long timescales.

5.3 Implications for fault mapping

Our results demonstrate that as surface ruptures degrade, not only do individual scarps become less pronounced, but also the overall fault zone width narrows significantly over time. This has important implications for fault mapping in arid environments. When mappers encounter shallow, softened, or isolated scarps, these features likely represent the remnants of a broader, more complex fault zone that has partially eroded (e.g., Zinke et al., 2015). The visible surface features are an incomplete record of the original rupture geometry. The degree of information loss varies substantially depending on the complexity of the original surface rupture — simple, single-strand fault zones retain mappable traces far longer than complex, multi-strand zones where distributed secondary scarps erode rapidly.

This limitation applies to both field-based and remote mapping efforts, but it may be even more consequential for remote mappers who rely on topographic data. Subtle features are often harder to detect in imagery and may fall below the threshold of visibility and mappability depending on data resolution. Even automated detection methods, such as deep learning models trained on high-resolution lidar or SfM data, rely on the presence of discernible landforms and perform best on fresh ruptures (e.g., Sare et al., 2019). As a result, mapped fault traces based on degraded landforms likely underestimate the true rupture width, distributed deformation, and rupture connectivity. Similar observations have been made in humid, high-relief environments, where faults with low slip rates or small cumulative offsets fall below a "geomorphic detectability threshold" and remain unmapped despite having produced surface ruptures (Kaneda, 2003). While the timescales and erosional mechanisms differ, our results show that even in low-relief arid landscapes, surface processes can erase secondary scarps and also lead to underrepresentation in fault maps fairly soon after the rupture ($\approx kt > 10^3\ m^2$). These findings reinforce the need to account for landform degradation in interpreting fault zone structure and to consider that unmappable scarps have likely been lost to surface processes over time.

5.4 Implications for hazard assessment

Understanding how fault scarps evolve provides critical constraints for hazard assessments. Mappable line length and fault zone width analyses show that isolated, secondary faults with small vertical displacements—often responsible for broadening the mapped fault zone—disappear from the record soon after the earthquake (within $\sim kt < 10^3\ m^2$). Degraded fault traces can lead to underestimation of the fault zone width and the extent of distributed deformation, impacting PFDHA and seismic hazard assessments, especially on immature strike-slip faults such as those in the ECSZ,

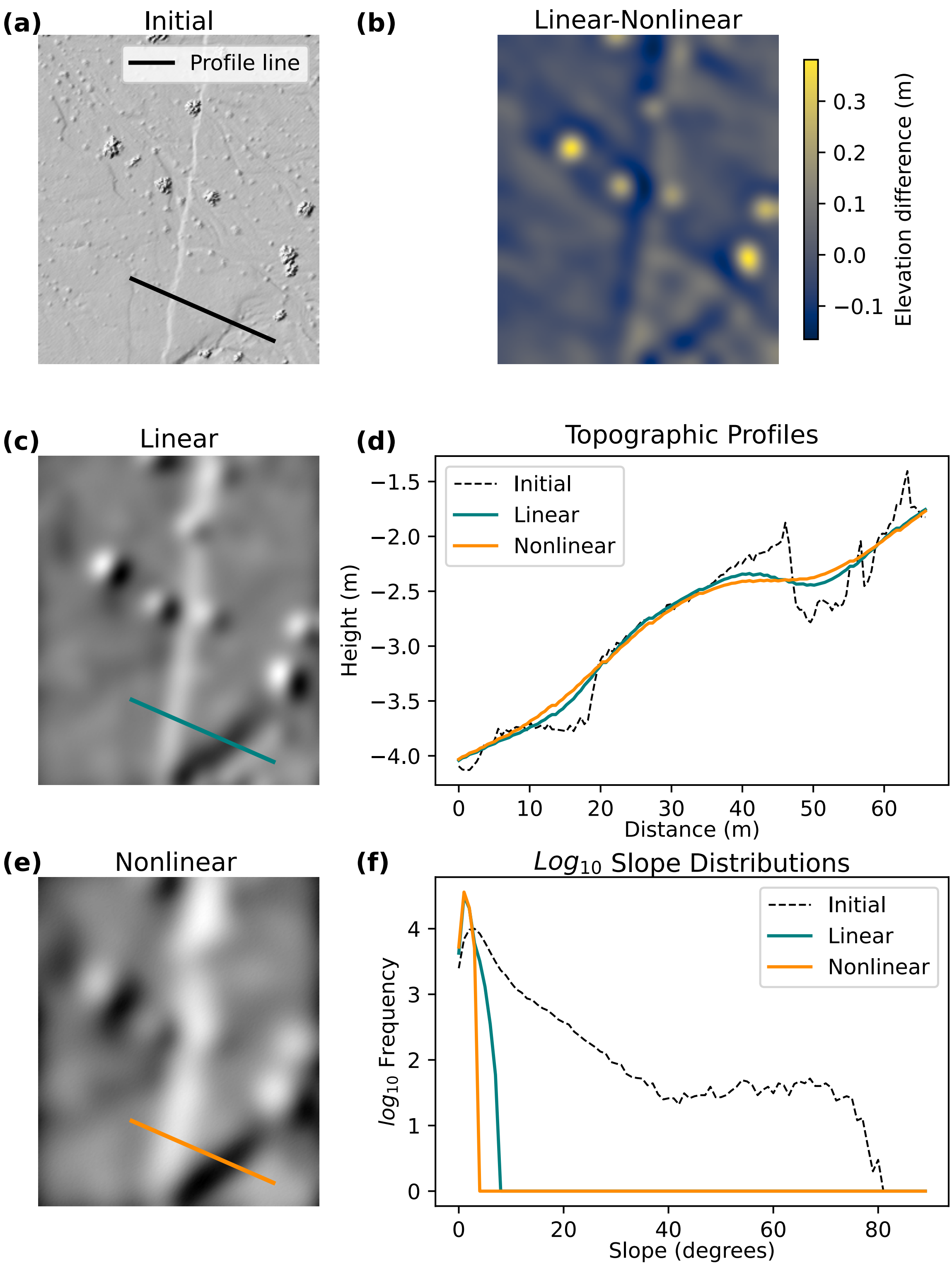

Figure 9 Simulated landscape change starting with original topography (A) with linear (B) and nonlinear (C) results (both $10\ m^2$; C uses n=0.5 from equation 8). (D) shows elevation difference for linear minus nonlinear. Same extent and scale as A, B, and C. Topographic profiles (E: location on A, B, C) show a greater change with the nonlinear case. (F) $\log_{10}$ slope distributions show the loss of steep topography in both cases and the lower modal slope in the nonlinear case. Simulations used de' Michieli Vitturi and Arrowsmith (2013) code.

where distributed fracturing is an important component of hazard (Rodriguez Padilla and Oskin, 2023).

Taken together, these findings suggest that while geomorphic traces of rupture may persist for long periods when their location is known, the ability to anticipate future rupture location from degraded landscapes remains limited. The difference reflects the contrast between retrospective degradation modeling (this study) and prospective rupture prediction from pre-event geomorphology (e.g., Petersen et al., 2011; Scott et al.,

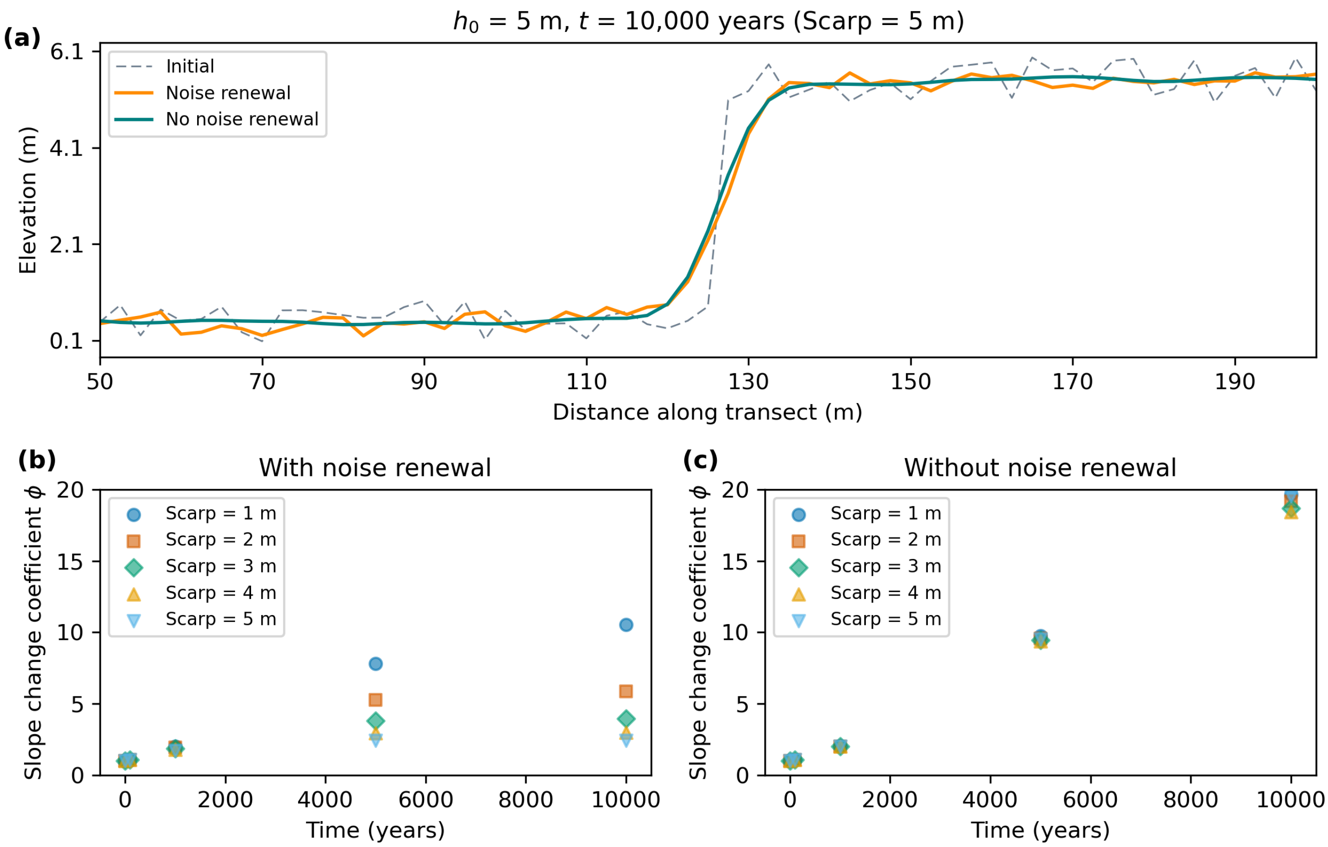

Figure 10 Degradation of a synthetic scarp with noise renewal and no noise renewal. A: A synthetic 5 m scarp linearly diffused with random noise applied on every time step (noise renewal in orange) and random noise only in the initial setting (in blue). Plots of the effect of (B) noise renewal and (C) no noise renewal on linearly diffused synthetic scarps of heights of 1–5 m over our timesteps (0, 100, 1k, 5k, and 10k years).

2023).

Thus, understanding how the record of vertical offset evolves with surface process action is a key step in constraining the availability of information for mapping at different timescales following an event (e.g., Petersen et al., 2011). Strike-slip earthquakes are characterized by vertical offsets along strike with gradients tied to fault geometry and incomplete rupture at depth (e.g., DuRoss et al., 2020). However, assuming low aleatory variability (the surface rupture patterns generally repeat), the larger scarps (which preserve relatively well) should indicate the location of future primary ruptures (e.g., Scott et al., 2024).

When modeling rupture zone degradation, the resolution of the elevation data must be considered. Too sparse elevation data will not resolve small vertical original displacements. High-resolution topographic data derived from lidar or photogrammetry at the meter scale or finer and systematic mapping approaches are essential for accurately capturing evidence of faulting, including small distributed ruptures (Arrowsmith and Zielke, 2009; Donnellan et al., 2017; Johnson et al., 2014).

Practitioners intuitively recognize the loss of information with time after an earthquake surface rupture. In addition, they demand an objective and easy to compute metric. Hence, we suggest that the slope change coefficient or similar topographic metrics may present an opportunity to reconstruct fault history over time. Where regional diffusivity k is independently constrained, ϕ could be forward-modeled to trace fault scarp evolution and quantify the extent of landform erasure, providing a crude estimate of elapsed time since fault activity in a reconnaissance mode. ϕ also may indicate whether the landforms are losing information rapidly or in steady state.

Mapping fault traces on degraded landscapes reveals challenges in fault mapping (e.g., Adam et al., 2025; Scott et al., 2023; Zuckerman et al., 2026b). Because we mapped landscapes from most to least degraded, we saw fault geomorphic indicators progressively come into focus. More degraded landscapes are blurry and contain continuous fault scarps. Younger landscapes revealed discontinuous primary fault traces and secondary fault traces splaying as much as 10–20 degrees from the main fault traces. Mitigating uncertainty in older fault scarp mapping involves considering wider fault zones and assuming additional distributed ruptures lost to surface processes (Figure 1).

6 Conclusions

This research highlights the dynamic nature of the landscapes along active fault zones and the indicative scarps and their degradation over time. We used a simple landscape evolution model to simulate landscape change following earthquakes and recorded the resulting change in mappable fault traces across 20 sites from the 2019 Ridgecrest and 2010 El Mayor-Cucapah ruptures, simulated over 10,000 years with a linear diffusivity of 1 m^2/kyr.

Across all study locations, 20–80% of the original mapped fault trace length remains after 10,000 years, with the rate of loss greatest in the first 100 years. For simple, single-strand fault zones, roughly 72% of the original trace length remains mappable at 10,000 years, and fault zone width narrows from a few meters to a single strand. For complex, multi-strand fault zones, up to 77% of mappable length is lost between 1,000 and 10,000 years, as distributed secondary traces erode rapidly and only a primary strand persists. On average across all 20 sites, mean fault zone width decreases from ~40 m to ~2 m over 10,000 years, converging toward a single mappable trace. This progressive narrowing means that older rupture zones appear simpler and more localized than they originally were, causing fault maps to systematically underestimate rupture width and complexity.

The slope change coefficient ϕ, defined as the ratio of the 68^{th} percentile of the slope distribution at the time of scarp formation to that at a later time (equation 4), is a simple topographic metric that may be useful to assess the degradation state of a faulted landscape. Where regional diffusivity k is known, ϕ could be forward-modeled to provide a crude estimate of elapsed time since fault activity or the degree of landform erasure. Direct empirical calibration would require repeat high-resolution topographic surveys spanning sufficient time for measurable landscape change, which remains a challenge given slow diffusion rates in arid environments. Future work could expand on this metric by applying empirical noise derived from real landscapes, using spectral analysis to isolate the scarp signal from erosional features such as rills, or leveraging repeat high-resolution topographic surveys to directly observe landscape change.

This work offers insights for fault-based seismic hazard analysis through modeling and field-based validation efforts. It provides concepts and suggests products to quantify the information loss for mapping faults and measuring rupture continuity, widths, lengths, and displacements. Recognizing that degraded landscapes underrepresent the original fault zone width and rupture complexity is essential for interpreting the geologic record, improving probabilistic fault displacement hazard models, and anticipating the full extent of distributed deformation along faults without recent surface-rupturing events.

Acknowledgements

This work was funded by NEHRP award G23AP00391. We thank Zhiang Chen, Madeline Schwarz, and River Sobzak for their help in the field. We thank Chelsea Scott for helpful discussions, and editor Randolph Williams and reviewers Nadine Reitman and Christoph Grützner for suggestions that improved the clarity and quality of this manuscript.

Data and code availability

The degradation and analysis Python code and the synthetic DEMs are available from Zenodo (Zuckerman et al., 2026a), and our 2024 Ridgecrest DEM is available from OpenTopography (Zuckerman et al., 2025). The code is also available from the GitHub repository.

Competing interests

The authors declare no competing interests.

References

Adam, R. N., Scott, C., Arrowsmith, J. R., Reano, D., Madugo, C., Koehler, R. D., Zuckerman, M. G., Gray, B., Kozaci, O., González, T., AbramsonWard, H., Rockwell, T. K., Gath, E., Kottke, A. R., and Leuchter, E. A systematic approach to mapping tectonic faults and documenting supporting geomorphology. *Geosphere*, 21 (2):227–244, Apr. 2025. doi: 10.1130/GES02767.1.

Andrews, D. J. and Hanks, T. C. Scarp degraded by linear diffusion: Inverse solution for age. *Journal of Geophysical Research: Solid Earth*, 90(B12):10193–10208, Oct. 1985. doi: 10.1029/JB090iB12p10193.

Arrowsmith, J. R. and Rhodes, D. D. Original forms and initial modifications of the Galway Lake Road scarp formed along the Emerson Fault during the 28 June 1992 Landers, California, Earthquake. *Bulletin of the Seismological Society of America*, 84(3): 511–527, 1994.

Arrowsmith, J. R. and Zielke, O. Tectonic geomorphology of the San Andreas Fault zone from high resolution topography: An example from the Cholame segment. *Geomorphology*, 113(1-2): 70–81, Dec. 2009. doi: 10.1016/j.geomorph.2009.01.002.

Arrowsmith, J. R., Pollard, D. D., and Rhodes, D. D. Hillslope development in areas of active tectonics. *Journal of Geophysical Research: Solid Earth*, 101(B3):6255–6275, Mar. 1996. doi: 10.1029/95JB02583.

Arrowsmith, J. R., Rhodes, D. D., and Pollard, D. D. Morphologic dating of scarps formed by repeated slip events along the San Andreas Fault, Carrizo Plain, California. *Journal of Geophysical Research: Solid Earth*, 103(B5):10141–10160, May 1998. doi: 10.1029/98JB00505.

Barnhart, K. R., Hutton, E. W. H., Tucker, G. E., Gasparini, N. M., Istanbulluoglu, E., Hobley, D. E. J., Lyons, N. J., Mouchene, M., Nudurupati, S. S., Adams, J. M., and Bandaragoda, C. Short communication: Landlab v2.0: a software package for Earth surface dynamics. *Earth Surface Dynamics*, 8(2):379–397, May 2020. doi: 10.5194/esurf-8-379-2020.

Brandenberg, S. J., Stewart, J. P., Wang, P., Nweke, C. C., Hudson, K., Goulet, C. A., Meng, X., Davis, C. A., Ahdi, S. K., Hudson, M. B., Donnellan, A., Lyzenga, G., Pierce, M., Wang, J., Winters, M. A., Delisle, M.-P., Lucey, J., Kim, Y., Gallien, T. W., Lyda, A., Yeung, J. S., Issa, O., Buckreis, T., and Yi, Z. Ground Deformation Data from GEER Investigations of Ridgecrest Earthquake Sequence. *Seismological Research Letters*, 91(4):2024–2034, July 2020. doi: 10.1785/0220190291.

de' Michieli Vitturi, M. and Arrowsmith, J. R. Two-dimensional nonlinear diffusive numerical simulation of geomorphic modifications to cinder cones. *Earth Surface Processes and Landforms*, 38(12):1432–1443, Sept. 2013. doi: 10.1002/esp.3423.

Dietrich, W. E., Bellugi, D. G., Sklar, L. S., Stock, J. D., Heimsath, A. M., and Roering, J. J. Geomorphic Transport Laws for Predicting Landscape form and Dynamics. In Wilcock, P. R. and Iverson, R. M., editors, *Geophysical Monograph Series*, pages 103–132.

American Geophysical Union, Washington, D. C, Mar. 2003. doi: 10.1029/135GM09.

Donnellan, A., Arrowsmith, R., and DeLong, S. Spatio-Temporal Mapping of Plate Boundary Faults in California Using Geodetic Imaging. *Geosciences*, 7(1):15, Mar. 2017. doi: 10.3390/geosciences7010015.

DuRoss, C. B., Gold, R. D., Dawson, T. E., Scharer, K. M., Kendrick, K. J., Angster, S. J., Bachhuber, J., Bacon, S., Bennett, S. E. K., Blair, L., Brooks, B. A., Bullard, T., Burgess, W. P., Chupik, C., DeFrisco, M., Delano, J., Dolan, J. F., Frost, E., Haddon, E. K., Hatem, A. E., Hernandez, J. L., Hitchcock, C., Hudnut, K., Jobe, J. T., Koehler, R., Kozaci, O., Ladinsky, T., Madugo, C., Milliner, C., Morelan, A., Olson, B., Patton, J., Philibosian, B., Pierce, I., Ponti, D. J., Seitz, G., Spangler, E., Swanson, B., Thomas, K., Valencia, F., Williams, A., and Zinke, R. Surface Displacement Distributions for the July 2019 Ridgecrest, California, Earthquake Ruptures. *Bulletin of the Seismological Society of America*, page 19, 2020.

Fletcher, J. M., Teran, O. J., Rockwell, T. K., Oskin, M. E., Hudnut, K. W., Mueller, K. J., Spelz, R. M., Akciz, S. O., Masana, E., Faneros, G., Fielding, E. J., Leprince, S., Morelan, A. E., Stock, J., Lynch, D. K., Elliott, A. J., Gold, P., Liu-Zeng, J., González-Ortega, A., Hinojosa-Corona, A., and González-García, J. Assembly of a large earthquake from a complex fault system: Surface rupture kinematics of the 4 April 2010 El Mayor–Cucapah (Mexico) Mw 7.2 earthquake. *Geosphere*, 10(4):797–827, Aug. 2014. doi: 10.1130/GES00933.1.

Ganti, V., Passalacqua, P., and Foufoula-Georgiou, E. A sub-grid scale closure for nonlinear hillslope sediment transport models. *Journal of Geophysical Research: Earth Surface*, 117(F2): 2011JF002181, June 2012. doi: 10.1029/2011JF002181.

Gray, H., Doane, T., Nicovich, S., Primus, M., DuRoss, C., and Gold, R. Evidence for nonlocal sediment transport on hillslopes from fault scarp morphology. *Geology*, 53(4):323–327, Apr. 2025. doi: 10.1130/G52987.1.

Hanks, T. C. The age of scarplike landforms from diffusion-equation analysis. In Stratton Noller, J., Sowers, J. M., and Lettis, W. R., editors, *Quaternary Geochronology: Methods and Application*, pages 313–338. American Geophysical Union (AGU), 2000. doi: 10.1029/RF004p0313.

Hanks, T. C., Bucknam, R. C., Lajoie, K. R., and Wallace, R. E. Modification of wave-cut and faulting-controlled landforms. *Journal of Geophysical Research*, 89(B7):5771–5790, 1984.

Hobley, D. E. J., Adams, J. M., Nudurupati, S. S., Hutton, E. W. H., Gasparini, N. M., Istanbulluoglu, E., and Tucker, G. E. Creative computing with Landlab: an open-source toolkit for building, coupling, and exploring two-dimensional numerical models of Earth-surface dynamics. *Earth Surface Dynamics*, 5(1):21–46, Jan. 2017. doi: 10.5194/esurf-5-21-2017.

Hudnut, K. W., Brooks, B. A., Scharer, K., Hernandez, J. L., Dawson, T. E., Oskin, M. E., Ramon Arrowsmith, J., Goulet, C. A., Blake, K., Boggs, M. L., Bork, S., Glennie, C. L., Fernandez-Diaz, J. C., Singhania, A., Hauser, D., and Sorhus, S. Airborne Lidar and Electro-Optical Imagery along Surface Ruptures of the 2019 Ridgecrest Earthquake Sequence, Southern California. *Seismological Research Letters*, Apr. 2020. doi: 10.1785/0220190338.

Johnson, K., Nissen, E., Saripalli, S., Arrowsmith, J. R., McGarey, P., Scharer, K., Williams, P., and Blisniuk, K. Rapid mapping of ultrafine fault zone topography with structure from motion. *Geosphere*, 10(5):969–986, Oct. 2014. doi: 10.1130/GES01017.1.

Johnstone, S. A. and Hilley, G. E. Lithologic control on the form of soil-mantled hillslopes. *Geology*, 43(1):83–86, Jan. 2015. doi: 10.1130/G36052.1.

Kaneda, H. Threshold of geomorphic detectability estimated from geologic observations of active low slip-rate strike-slip faults. *Geophysical Research Letters*, 30(5), Mar. 2003. doi: 10.1029/2002gl016280.

Koehler, R. D., Dee, S., Elliott, A., Hatem, A., Pickering, A., Pierce, I., and Seitz, G. Field response and surface-rupture characteristics of the 2020 M 6.5 Monte Cristo range earthquake, central Walker Lane, Nevada. *Seismological Research Letters*, 92(2A):823–839, Mar. 2021. doi: 10.1785/0220200371.

Moss, R. E. S. and Ross, Z. E. Probabilistic Fault Displacement Hazard Analysis for Reverse Faults. *Bulletin of the Seismological Society of America*, 101(4):1542–1553, Aug. 2011. doi: 10.1785/0120100248.

Nash, D. B. Morphologic dating of fluvial terrace scarps and fault scarps near West Yellowstone, Montana. *Geological Society of America Bulletin*, 95(12):1413, 1984. doi: 10.1130/0016-7606(1984)95<1413:MDOFTS>2.0.CO;2.

Nurminen, F., Baize, S., Boncio, P., Blumetti, A. M., Cinti, F. R., Civico, R., and Guerrieri, L. SURE 2.0 – New release of the worldwide database of surface ruptures for fault displacement hazard analyses. *Scientific Data*, 9(1):729, Nov. 2022. doi: 10.1038/s41597-022-01835-z.

OpenTopography. El Mayor-Cucapah Earthquake (4 April 2010) Rupture LiDAR Scan, 2010. doi: 10.5069/G9TD9V7D. Accessed 17 Nov 2024.

Petersen, M. D., Dawson, T. E., Chen, R., Cao, T., Wills, C. J., Schwartz, D. P., and Frankel, A. D. Fault displacement hazard for strike-slip faults. *Bulletin of the Seismological Society of America*, 101(2):805–825, Apr. 2011. doi: 10.1785/0120100035.

Pierce, I., Williams, A., Koehler, R. D., and Chupik, C. High-resolution Structure-from-Motion models and orthophotos of the Southern Sections of the 2019 Mw 7.1 and 6.4 Ridgecrest Earthquakessurface ruptures. *Seismological Research Letters*, 91(4):2124–2126, July 2020. doi: 10.1785/0220190289.

Pierce, K. L. and Colman, S. M. Effect of height and orientation (microclimate) on geomorphic degradation rates and processes, late-glacial terrace scarps in central Idaho. *Geological Society of America Bulletin*, 97(7):869, 1986. doi: 10.1130/0016-7606(1986)97<869:EOHAOM>2.0.CO;2.

Ponti, D. J., Blair, J. L., Rosa, C. M., Thomas, K., Pickering, A. J., Akciz, S., Angster, S., Avouac, J.-P., Bachhuber, J., Bacon, S., Barth, N., Bennett, S., Blake, K., Bork, S., Brooks, B., Bullard, T., Burgess, P., Chupik, C., Dawson, T., DeFrisco, M., Delano, J., DeLong, S., Dolan, J., Donnellan, A., DuRoss, C., Ericksen, T., Frost, E., Funning, G., Gold, R., Graehl, N., Gutierrez, C., Haddon, E., Hatem, A., Helms, J., Hernandez, J., Hitchcock, C., Holland, P., Hudnut, K., Kendrick, K., Koehler, R., Kozaci, O., Ladinsky, T., Leeper, R., Madugo, C., Mareschal, M., McDonald, J., McPhillips, D., Milliner, C., Mongovin, D., Morelan, A., Nale, S., Nevitt, J., O'Neal, M., Olson, B., Oskin, M., Padilla, S., Patton, J., Philibosian, B., Pierce, I., Pridmore, C., Roth, N., Sandwell, D., Scharer, K., Seitz, G., Singleton, D., Smith-Konter, B., Spangler, E., Swanson, B., Jobe, J. T., Treiman, J., Valencia, F., Vanderwal, J., Williams, A., Xu, X., Zachariasen, J., Zimmerman, J., and Zinke, R. Documentation of surface fault rupture and ground-deformation features produced by the 4 and 5 July 2019 Mw 6.4 and Mw 7.1 Ridgecrest earthquake sequence. *Seismological Research Letters*, 91(5):2942–2959, Sept. 2020a. doi: 10.1785/0220190322.

Ponti, D. J., Pickering, A. J., Blair, J. L., Rosa, C. M., Thomas, K., and Dawson, T. Digital datasets documenting surface fault rupture and ground deformation features produced by the Ridgecrest M6.4 and M7.1 earthquake sequence of July 4 and 5, 2019, 2020b. doi: 10.5066/P9BZ5IJ9.

Reitman, N. G., Mueller, K. J., Tucker, G. E., Gold, R. D., Briggs, R. W., and Barnhart, K. R. Offset channels may not accurately record strike-slip fault displacement: evidence from landscape evolution models. *Journal of Geophysical Research: Solid Earth*, 124 (12):13427–13451, 2019. doi: 10.1029/2019JB018596.

Rockwell, T. K., Fletcher, J. M., Teran, O. J., Hernandez, A. P., Mueller, K. J., Salisbury, J. B., Akciz, S. O., and Štěpančíková, P. Reassessment of the 1892 Laguna Salada Earthquake: Fault Kinematics and Rupture Patterns. *Bulletin of the Seismological Society of America*, 105(6):2885–2893, Dec. 2015. doi: 10.1785/0120140274.

Rodriguez Padilla, A. M. and Oskin, M. Displacement hazard from distributed ruptures in strike-slip earthquakes. *Bulletin of the Seismological Society of America*, 113(6), July 2023. doi: 10.1785/0120230044.

Rodriguez Padilla, A. M., Quintana, M. A., Prado, R. M., Aguilar, B. J., Shea, T. A., Oskin, M. E., and Garcia, L. Near-Field High-Resolution Maps of the Ridgecrest Earthquakes from Aerial Imagery. *Seismological Research Letters*, 93(1):494–499, Jan. 2022. doi: 10.1785/0220210234.

Roering, J. J., Kirchner, J. W., and Dietrich, W. E. Evidence for nonlinear, diffusive sediment transport on hillslopes and implications for landscape morphology. *Water Resources Research*, 35 (3):853–870, Mar. 1999. doi: 10.1029/1998WR900090.

Sare, R., Hilley, G. E., and DeLong, S. B. Regional-scale detection of fault scarps and other tectonic landforms: examples from northern California. *Journal of Geophysical Research: Solid Earth*, 124(1):1016–1035, Jan. 2019. doi: 10.1029/2018JB016886.

Sarmiento, A., Madugo, D., Shen, A., Dawson, T., Madugo, C., Thompson, S., Bozorgnia, Y., Baize, S., Boncio, P., Kottke, A., Lavrentiadis, G., Mazzoni, S., Milliner, C., Nurminen, F., and Visini, F. Database for the Fault Displacement Hazard Initiative project. *Earthquake Spectra*, page 87552930241262766, July 2024. doi: 10.1177/87552930241262766.

Sarmiento, A., Lavrentiadis, G., Bozorgnia, Y., Chen, R., Chiou, B., Dawson, T., Kottke, A., Kuehn, N., Madugo, C., Moss, R., Thompson, S., and Zandieh, A. Comparisons of FDHI fault displacement models for principal and aggregate displacement. *Earthquake Spectra*, 41(4):2691–2720, Nov. 2025. doi: 10.1177/87552930251327894.

Schmitt, R. G., Gold, R. D., and Geologic Hazards Science Center. Quaternary Fault and Fold Database for the nation, 2020. doi: 10.5066/P9BCVRCK.

Scott, C., Adam, R., Arrowsmith, R., Madugo, C., Powell, J., Ford, J., Gray, B., Koehler, R., Thompson, S., Sarmiento, A., Dawson, T., Kottke, A., Young, E., Williams, A., Kozaci, O., Oskin, M., Burgette, R., Streig, A., Seitz, G., Page, W., Badin, C., Carnes, L., Giblin, J., McNeil, J., Graham, J., Chupik, D., and Ingersoll, S. Evaluating how well active fault mapping predicts earthquake surface-rupture locations. *Geosphere*, June 2023. doi: 10.1130/GES02611.1.

Scott, C., Kottke, A., Madugo, C., Arrowsmith, J. R., Adam, R., and Zuckerman, M. Tectonic landform and lithologic age impact uncertainties in fault displacement hazard models. *Geophysical Research Letters*, 51(16):e2024GL109145, Aug. 2024. doi: 10.1029/2024GL109145.

Thompson Jobe, J. A. and Reitman, N. G. Timescales of surface faulting preservation in low-strain intraplate regions from landscape evolution modeling and the geomorphic and historical record. *Journal of Geophysical Research: Solid Earth*, 130(6), June 2025. doi: 10.1029/2024jb029966.

Wallace, R. E. The San Andreas Fault System, California. Professional Paper 1515, US Geological Survey, 1990. Series: Professional Paper.

Waskom, M. seaborn: statistical data visualization. *Journal of Open Source Software*, 6(60):3021, Apr. 2021. doi: 10.21105/joss.03021.

Xu, J., Arrowsmith, J. R., Chen, J., Schoenbohm, L. M., Li, T., Yuan, Z., and Owen, L. A. Evaluating young fluvial terrace riser degradation using a nonlinear transport model: Application to the Kongur Normal Fault in the Pamir, northwest China. *Earth Surface Processes and Landforms*, 46(1):280–295, Jan. 2021. doi: 10.1002/esp.5022.

Young, E. K., Oskin, M. E., and Rodriguez Padilla, A. M. Reproducibility of remote mapping of the 2019 Ridgecrest earthquake surface ruptures. *Seismological Research Letters*, 95(1):288–298, Jan. 2024. doi: 10.1785/0220230095.

Youngs, R. R., Arabasz, W. J., Anderson, R. E., Ramelli, A. R., Ake, J. P., Slemmons, D. B., McCalpin, J. P., Doser, D. I., Fridrich, C. J., Swan, F. H., Rogers, A. M., Yount, J. C., Anderson, L. W., Smith, K. D., Bruhn, R. L., Knuepfer, P. L. K., Smith, R. B., dePolo, C. M., O'Leary, D. W., Coppersmith, K. J., Pezzopane, S. K., Schwartz, D. P., Whitney, J. W., Olig, S. S., and Toro, G. R. A methodology for Probabilistic Fault Displacement Hazard Analysis (PFDHA). *Earthquake Spectra*, 19(1):191–219, Feb. 2003. doi: 10.1193/1.1542891.

Zinke, R., Dolan, J. F., Van Dissen, R., Grenader, J. R., Rhodes, E. J., McGuire, C. P., Langridge, R. M., Nicol, A., and Hatem, A. E. Evolution and progressive geomorphic manifestation of surface faulting: A comparison of the Wairau and Awatere faults, South Island, New Zealand. *Geology*, 43(11):1019–1022, Nov. 2015. doi: 10.1130/g37065.1.

Zuckerman, M. G., Rodriguez Padilla, A. M., and Arrowsmith, J. R. High-Res SfM Topography of a Portion of the 2019 M7.1 Ridgecrest Rupture, 2025. doi: 10.5069/G9TT4P5P.

Zuckerman, M. G., Rodriguez Padilla, A. M., and Arrowsmith, J. R. Quantifying the erasure of earthquake surface ruptures from desert landscapes: Implications for seismic hazard assessment [dataset], 2026a. doi: 10.5281/zenodo.10652347.

Zuckerman, M. G., Scott, C. P., Arrowsmith, J. R., Adam, R. N., Madugo, C., Koehler, R. D., Kottke, A., AbramsonWard, H., Gath, E., Gonzalez, T., Gray, B., Kozaci, O., Rockwell, T. K., Austin, T. J., King, T., Micander, R., Leuchter, E., Pierce, I., Alexander, E., Gourdeau, A., Laly, M., Ogilvie, I., Rothman, S. D., Vlaha, D., Young, E. K., Prush, V., Rowe, C., Johnson, B., and Schwarz, M. The impact of experience and data on the quality of geomorphic fault mapping. *Seismica*, 5(2), 2026b. doi: 10.26443/seismica.v5i2.1973.